OPEN ACCESS
IOP Publishing

Plasma Physics and Controlled Fusion

Plasma Phys. Control. Fusion **62** (2020) 115024 (15pp)

https://doi.org/10.1088/1361-6587/abb24e

High-current laser-driven beams of relativistic electrons for high energy density research

O N Rosmej[1,2], M Gyrdymov[2], M M Günther[1], N E Andreev[3,4], P Tavana[2], P Neumayer[1], S Zähter[1,2], N Zahn[2], V S Popov[3,4], N G Borisenko[5], A Kantsyrev[6], A Skobliakov[6], V Panyushkin[6], A Bogdanov[6], F Consoli[7], X F Shen[8] and A Pukhov[8]

[1] GSI Helmholtzzentrum für Schwerionenforschung GmbH, Planckstr.1, 64291, Darmstadt, Germany
[2] Goethe University Frankfurt, Max-von-Laue-Str. 1, 60438, Frankfurt am Main, Germany
[3] Joint Institute for High Temperatures, RAS, Izhorskaya st.13, Bldg. 2, 125412, Moscow, Russia
[4] Moscow Institute of Physics and Technology (State University), Institutskiy Pereulok 9, 141700, Dolgoprudny Moscow Region, Russia
[5] P. N. Lebedev Physical Institute, RAS, Leninsky Prospekt 53, 119991, Moscow, Russia
[6] Institute for Theoretical and Experimental Physics named by A. I. Alikhanov of NRC 'Kurchatov Institute', B. Cheremuschkinskaya 25, 117218, Moscow, Russia
[7] ENEA. Fusion and Nuclear Safety Department, C.R. Frascati, Via Enrico Fermi, 45, 00044, Frascati, Italy
[8] Heinrich-Heine-University Düsseldorf, Universitätsstraße 1, Düsseldorf, Germany

E-mail: o.rosmej@gsi.de

Received 2 July 2020, revised 13 August 2020
Accepted for publication 25 August 2020
Published 12 October 2020

Abstract

We report on enhanced laser driven electron beam generation in the multi MeV energy range that promises a tremendous increase of the diagnostic potential of high energy sub-PW and PW-class laser systems. In the experiment, an intense sub-picosecond laser pulse of $\sim 10^{19}$ Wcm^{-2} intensity propagates through a plasma of near critical electron density (NCD) and drives the direct laser acceleration (DLA) of plasma electrons. Low-density polymer foams were used for the production of hydrodynamically stable long-scale NCD-plasmas. Measurements show that relativistic electrons generated in the DLA-process propagate within a half angle of $12 \pm 1^\circ$ to the laser axis. Inside this divergence cone, an effective electron temperature of 10–13 MeV and a maximum of the electron energy of 100 MeV were reached. The high laser energy conversion efficiency into electrons with energies above 2 MeV achieved 23% with a total charge approaching 1 μC. For application purposes, we used the nuclear activation method to characterize the MeV bremsstrahlung spectrum produced in the interaction of the high-current relativistic electrons with high-Z samples and measured top yields of gamma-driven nuclear reactions. The optimization of the high-Z target geometry predicts an ultra-high MeV photon number of $\sim 10^{12}$ per shot at moderate relativistic laser intensity of 10^{19} Wcm^{-2}. A good agreement between the experimental data and the results of the 3D-PIC and GEANT4-simulations was demonstrated.

Keywords: relativistically intense laser pulses, near critical electron density plasmas, long-scale plasma channel, direct laser acceleration, low-density polymer aerogels, super-ponderomotive electrons, nuclear reaction yields

(Some figures may appear in colour only in the online journal)

1. Introduction

Laser-driven relativistic electron beams are excellent tools for the generation of ultrashort MeV- gammas [1–4], electron-positron pairs [5–7], neutrons [8], THz [9–11] and betatron [12–17] radiation. In the case of well-directed high current beams of relativistic electrons one can reach extreme high brightness of gamma and neutron sources and use them for radiographic applications in probing of high energy density matter [18, 19]. Another application can be found in the field of laser driven nuclear physics [20–22].

Two mechanisms of laser-driven acceleration are currently being discussed as promising for the generation of high energy electrons in near- and sub-critical plasmas. The first one is the laser wake field acceleration (LWFA) [23]: the intense laser pulse drives strong plasma waves that can trap and accelerate electrons. The most prominent case of LWFA is the so-called bubble regime [24–27]. The LWFA allows to reach the highest electron energies of 10 GeV [28] and finds its applications in high energy physics and potentially in XFEL devices [29–31]. The LWFA works best in tenuous, very under-dense plasmas and ultra-short laser pulses, shorter than the plasma wavelength.

The second mechanism is the direct laser acceleration (DLA) in a plasma channel created by a relativistic laser pulse [32]. In this case, the electron acceleration occurs in the presence of strong quasi-static electric and magnetic fields generated in plasma [32, 33]. Ponderomotive expulsion of background plasma electrons from the channel caused by a relativistic laser pulse creates a radial electrostatic field and at the same time, the current of accelerated electrons generates the azimuthal magnetic field [33–35]. A relativistic electron trapped in the channel experiences transverse betatron oscillations and gains energy efficiently from the laser pulse when the frequency of the betatron oscillations becomes resonant with the Doppler shifted laser frequency [33]. Depending on the plasma density and laser intensity, DLA at the betatron resonance, stochastic heating [36], transition to wake field acceleration or a combination of these mechanisms is realized.

The DLA works efficiently in near critical density (NCD) plasmas and for sub-ps laser pulses like petawatt high energy laser for ion experiments (PHELIX) at GSI [37]. Different from LWFA, the DLA does not generate electrons at very high energies, rather, it produces ample amounts of electrons with Boltzmann-like distributions carrying mega-ampere currents. The effective temperature of these electrons can reach several tens of MeV. Interaction of these relativistic electrons with high Z materials causes MeV gamma-radiation that can drive nuclear reactions resulting in neutron production [8]. This scheme based on the laser accelerated electron beam is one of the important pillars of the laser driven nuclear physics program at ELI-NP [20].

Up to now, only a few experiments were performed to demonstrate the advantages of this DLA mechanism in plasmas of near critical electron density. The energy-transfer from an ultra-intense laser pulse with intensity of 10^{20} Wcm^{-2} to hot electrons in NCD plasmas depending on the pre-plasma scale- length was investigated in [38]. In this experiment, a one-dimensional expansion of the plasma with a well-controlled scale length was produced by a separate ns laser pulse. The energy distribution of energetic electrons was not measured but simulated using a 2D particle-in cell (PIC) code. A discovered one order of magnitude variation in the coupling efficiency of the laser energy into fast electrons, defined via measurements of the Cu-K$_\alpha$, was explained by the existence of a density gradient optimum that ensures strong laser pulse self-focusing and channeling processes. In [39], measurements of electrons accelerated by a relativistic laser pulse propagating across a mm-long extended under-dense plasma plume with (0.02–0.05) × 10^{21} cm^{-3} were reported. The experiment showed a strong increase of the effective temperature and a number of super-ponderomotive electrons caused by the increased length of a relativistic plasma channel. New results on the electron acceleration from an ASE pre-pulse pre-ionized foam layers conducted at the Omega EP-laser were reported in [35]. Foam layers of 250 μm thickness and 3 up to 100 mg cm^{-3} ($n_e = (0.9–30) \times 10^{21}$ cm^{-3}) mean densities were used as targets. The 1 kJ short laser pulse had $(5.3 \pm 1.8) \times 10^{19}$ Wcm^{-2} intensity. An approximation of the high energy tail of the measured electron spectra by a Maxwellian-like function resulted in an effective electron temperature, of 6–8 MeV averaged over several shots. Measurements in the case of foam layers with high areal densities did not show a visible effect toward an increased electron temperature. The drawback of this experiment is that the intensity and the duration of the ASE pre-pulse were not adapted to the variety of the used foam densities.

The production of a hydrodynamically stable NCD-plasma layer remains an important issue. A low density polymer aerogel [42] is a very prospective material for the creation of sub-mm long NCD-plasmas and efficient electron acceleration. In [43], polymer foams of 300–500 μm thickness and 2 mg cm^{-3} mean volume density were used as targets. In foams, the NCD-plasma was produced by a mechanism of super-sonic ionization [44, 45] when a well-defined separate ns-pulse was sent onto the foam target forerunning the relativistic main pulse. The required intensity of the ns-pulse ($\sim 5 \times 10^{13}$ Wcm^{-2}) was estimated according to the reference

[44] in order to reach the velocity of the super-sonic ionization wave equal to ∼250 μm ns^{-1}. The created plasma had an electron density of $n_e = 0.7 \times 10^{21}$ cm^{-3}. The application of sub-mm thick low-density foam layers provided a substantial increase of the electron acceleration path in a NCD-plasma compared to the case of freely expanding plasmas created in the interaction of the ns-laser pulse with solid foils. In experiments described in [39], the interaction of sub-ps laser pulses of the moderate relativistic intensity interacted with standard metallic foils and pre-ionized low-density foam layers was investigated. The effective temperature of super-thermal electrons raised from 1.5–2 MeV, in the case of metallic foils, up to 13 MeV for the laser shots onto long-scale NCD-plasmas. The high conversion efficiency in the last case was confirmed by the results of the PIC-simulations [40, 43]. In [43] it was shown that up to 80% of the laser energy was converted into electrons, while up to 7% was absorbed by the C, O and H-ions.

In continuation of our research on the electron acceleration in long-scale NCD-plasmas described in [43], we present new results on the characterization of the super-ponderomotive electrons and demonstrate a big advantage of our approach for generation of ultra-bright gamma sources compared to the interaction of ultra-high intensity laser pulses with conventional foil targets. The experiment was supported by PIC and GEANT4 simulations.

The paper is organized as follows: laser and target parameters together with the used experimental set-up are described in details in section 2; Experimental results on characterization of super-ponderomotive electron beams are presented in section 3; in section 4, results of PIC-simulations, that account for the experimental geometry, are compared to the experiment; in section 5, the experimental and numerical results on the gamma-ray generation by the well-directed ultra-relativistic electron beams are discussed; section 6 summarizes the results.

2. Experimental set-up

Experiments were performed at the PHELIX at the Helmholtzzentrum GSI Darmstadt [37] at the highest ns laser contrast $\geq 10^{11}$. A s-polarized laser pulse of 1.053 μm fundamental wavelength delivered by the Nd:glass laser was sent onto targets at 5–7 degree to the target normal. Two different focusing off-axis parabolic mirrors were used providing peak laser intensities of (1–2.5) $\times$ 10^{19} Wcm^{-2} ($a_L = 2.7$–4.27) and (7–10) $\times$ 10^{20} Wcm^{-2} ($a_L = 22.6$–27.0). Here a_L is the normalized vector potential that scales as $a_L{}^2 = 0.73 \cdot I_{L,18} \cdot \lambda^2$ with the laser intensity $I_{L,18}$ normalized to 10^{18} Wcm^{-2} and the laser wavelength λ, in µm. The duration of the laser pulse was 750 ± 250 fs. In the case of a moderate relativistic laser intensity (1–2.5) $\times$ 10^{19} Wcm^{-2}, 90 ± 10 J laser energy measured after the main amplifier was focused by means of a 150 cm off-axis parabolic mirror into an elliptical focal spot with FWHM diameters 12 ± 2 μm and 18 ± 2 μm containing a laser energy of $E_{FWHM} \simeq$ (17–22) J. In the case of the ultra-relativistic laser intensity, 180 J laser energy was focused into a 2.7 ± 0.2 μm × 3.2 ± 0.2 µm focal spot by a 40 cm off-axis parabolic mirror. The laser energy in the focal spot was 20% of that after the main amplifier and reached $E_{FWHM} \simeq$ (36–40) J. The laser spot size on target and the laser energy in the focal spot were controlled in every shot. Experiments on the direct laser acceleration of electrons in plasmas of near critical density were performed using the mentioned off-axis parabolic mirror with a focal length of 150 cm. In the case of ultra-high laser intensity, shots were done only onto metallic foils.

Cellulose triacetate (TAC, $C_{12}H_{16}O_8$) layers of 2 mg cm^{-3} volume density and 300–400 μm thickness [42, 43] were used as targets [43]. In the case of fully ionized plasma, it corresponds to 0.64 $\times$ 10^{21} cm^{-3} electron density or 0.64 n_{cr}, where $n_{cr} = 10^{21}$ cm^{-3}. A sub-mm long NCD-plasma was produced by sending a well-controlled nanosecond pulse fore-running the relativistic main pulse onto a foam. The intensity of the ns laser pulse was kept at ∼5 $\times$ 10^{13} Wcm^{-2} level in order to initiate a super-sonic ionization wave propagating with 2 $\times$ 10^{7} cm s^{-1} velocity, see [44, 45] for more details. The ns-pulse was focused on target by the same parabolic mirror as the short pulse. Generation of a long scale NCD-plasma requires focusing optics with hundreds of micrometers long Rayleigh length that was the case for the 150 cm off-axis parabolic mirror. This ensures rather constant ns laser pulse intensity along the whole layer thickness. The delay between the peak of the ns-pulse and the relativistic main pulse was fixed by 2–3 ns. Experimental set-ups and a target holder with a low-density foam layer fixed inside a 2.5 mm in diameter Cu-washer are shown in (figure 1). In both set-ups, the electron spectra were measured simultaneously at three different angles with respect to the laser axis. The spectrometers were equipped with 0.99 T static magnets and imaging plates (IP) [48, 49] for the detection of the electron signal. The energy resolution of the spectrometers with 300 μm (width) × 1000 μm (height) entrance slits was numerically simulated using 2D B-field distributions measured inside the spectrometer steel-housing. It was shown that an experimental error in the energy measurements is caused mostly by the entrance slit and is not higher than 2%. This allows for reliably measuring of electron spectra from 1.75 up to 100 MeV. The spectrometers were placed in the horizontal plane *XOZ* (which is perpendicular to the laser polarization along *OY*) at a distance of 405 mm from the interaction point around the target at 0°, 15° and 45° (5–7 in figure 1(a)). Massive 20 up to 40 mm long WCu—collimator blocks with 3 mm entrance hole were placed in front of every spectrometer in order to shield the front plate from gamma-rays and to increase the signal-to-noise ratio.

The angular distribution of the electron beam in a wide range of angles was measured by means of a stack of three stainless steel cylindrical plates of 3 mm thickness each, rather similar to that described in [50]. The cylinder-stack had a curvature radius of 200 mm and was placed 230 mm away from the target position (4 in figure 1(a)). The observation angle was 0° ± 50° in the horizontal direction and 0° ± 15° in the vertical direction, where 0° corresponds to the laser axis. A horizontal 4 mm wide slit centered at the laser pulse height allowed for the electron propagation to the magnetic spectrometers placed behind the cylinder-stack. In order to

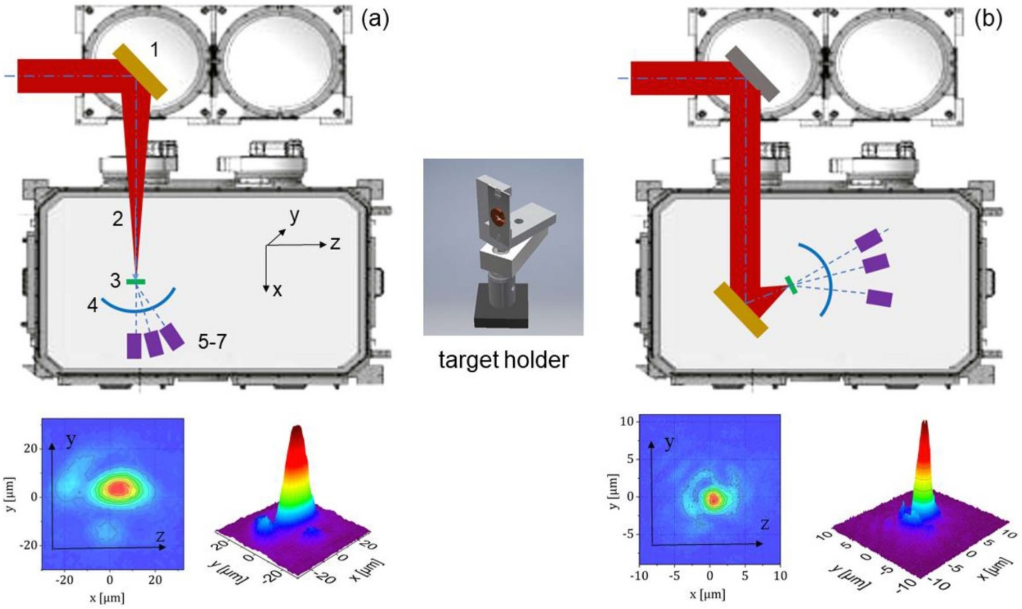

Figure 1. Experimental set-ups (top-view) used for shots (a) at moderate and (b) ultra-high relativistic intensities. Scheme (a) shows an off-axis focusing parabola (1), laser beam (2), target position (3), stack of cylinders (4), and three magnetic spectrometers (5 ÷ 7). The laser intensity distributions for both set-ups are also shown.

map the position of the electron beam in space, small holes with a 20 mm interval in vertical and horizontal directions were drilled into the front plate. Large area IPs were placed between the first and the second, and the second and the third cylindrical plates to map the spatial distribution of electrons with $E > 3$ MeV and $E > 7.5$ MeV respectively.

A nuclear activation-based diagnostic [51, 52] was used to characterize MeV bremsstrahlung radiation generated in the interaction of the super-ponderomotive electrons with high-Z materials. The activation samples, consisting of stacked together Au, Ta, In and Cr plates, were fixed at horizontal angles of 6° ± 1° and 16° ± 1° to the laser pulse axis (figures 2(b) and (d)). After irradiation by electrons and gammas, all activation samples were counted multiple times on a low background HPGe-detector to identify nuclides via known γ-ray energies, intensities, and half-life times. Reaction yields of the obtained isotopes $^{196\,194,192}$Au, ^{180,178m}Ta and ^{51,49}Cr produced due to photodisintegration were used for reconstruction of the MeV bremsstrahlung spectrum. A 0.25 mm thin In-foil was placed between Ta and Cr for measurements of the neutron yield [53].

3. Experimental results on high-current relativistic electrons

Figure 2 shows raw electron spectra measured in two selected laser shots at 0° with respect to the laser axis by means of the 0.99 T electron spectrometer and the angular distribution of the electron beam with $E > 3$ MeV and $E > 7.5$ MeV measured using the cylinder-stack. For registration of the electron signal Fuji BAS IP MS type was used as detector, while for diagnostic of the electron angular distribution Fuji BAS IP TR. For each picture in (figure 2), the maximum intensity of the related raw signals expressed in PSL (Photo Stimulated Luminescence) is indicated. The presented shots were made at $\sim 10^{19}$ Wcm^{-2} laser intensity onto a 10 μm thin Au-foil (figures 2(a) and (b)) and a pre-ionized foam combined with a 10 μm Au-foil attached to the rear side (figures 2(c) and (d)). In the case of the pre-ionized foam, the raw electron spectrum shows a 10-fold enhancement of the IP-signal (compare figures 2 (a) and (c)) that reflects a corresponding increase of the number of electrons with energies above 2 MeV [48]. In the case of the foil target, the maximum of the measured electron energy lays in the area up to 15 MeV, while for shots onto the pre-ionized foam stacked together with the Au-foil, the maximum electron energy reached 95–100 MeV.

For the shots onto NCD-plasmas, we observed by means of the cylinder-stack a strong collimation of electrons with energies $E > 3$ MeV (first IP) and $E > 7.5$ MeV (second IP) into a well-directed electron beam with a half of a divergence angle of 12° ± 1° at FWHM (figure 2(d)). The IP signal produced by electrons with energies higher than 3 MeV that could pass through the first 3 mm of stainless steel was oversaturated (>300 PSL), while the IP signal obtained for the laser shot onto foil reached only 8–10 PSL (figure 2(b)).

GEANT4 [56–58] simulations were performed to define the input of electrons and x-rays into the IP-image. The discussed experimental geometry (figure 1(a)), the measured electron energy distribution (figures 2(c), 5 and 0°) and the BAS IP TR imaging plate response to electrons and photons [48] were used as input parameters. Simulations showed that the contribution of photons to the IP signal is less than 5% and that the obtained signal can be attributed mainly to the electron angular distribution.

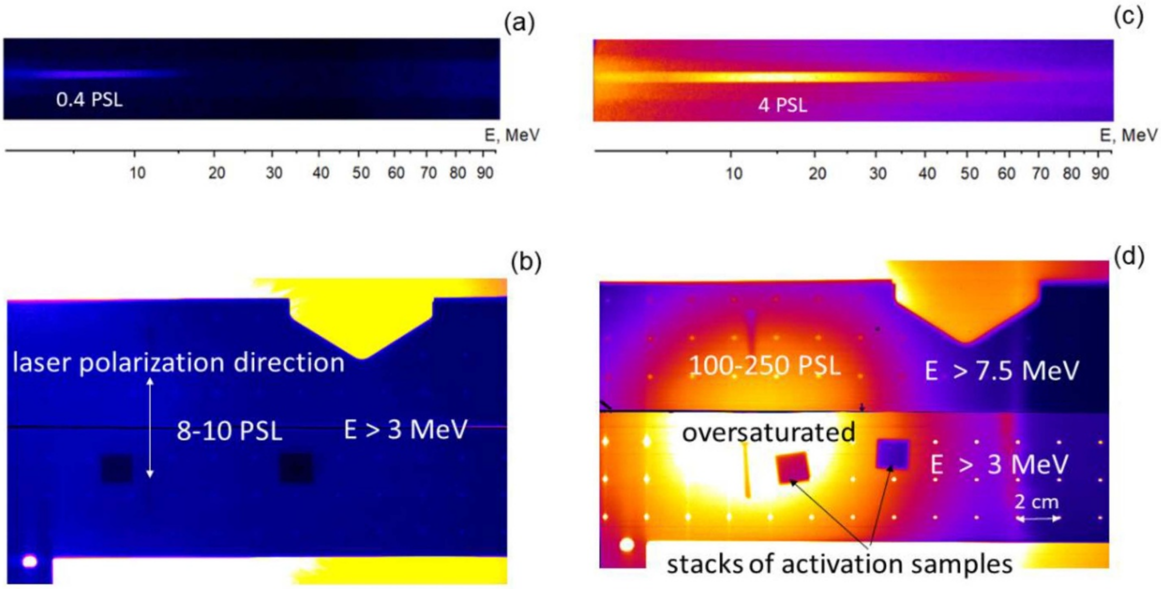

Figure 2. Raw electron spectra measured along the laser axis by means of the 0.99 T electron spectrometer (a, c) and angular distribution of the electron beam with E > 3 MeV and > 7.5 MeV registered using the cylinder-stack (b, d): (a, b) shot at 1.6 × 10^{19} Wcm^{-2} laser intensity onto a 10 μm thin Au-foil; (c, d) shot at 1.5 × 10^{19} Wcm^{-2} laser intensity onto pre-ionized foam layer of 325 μm thickness combined with a 10 μm Au-foil.

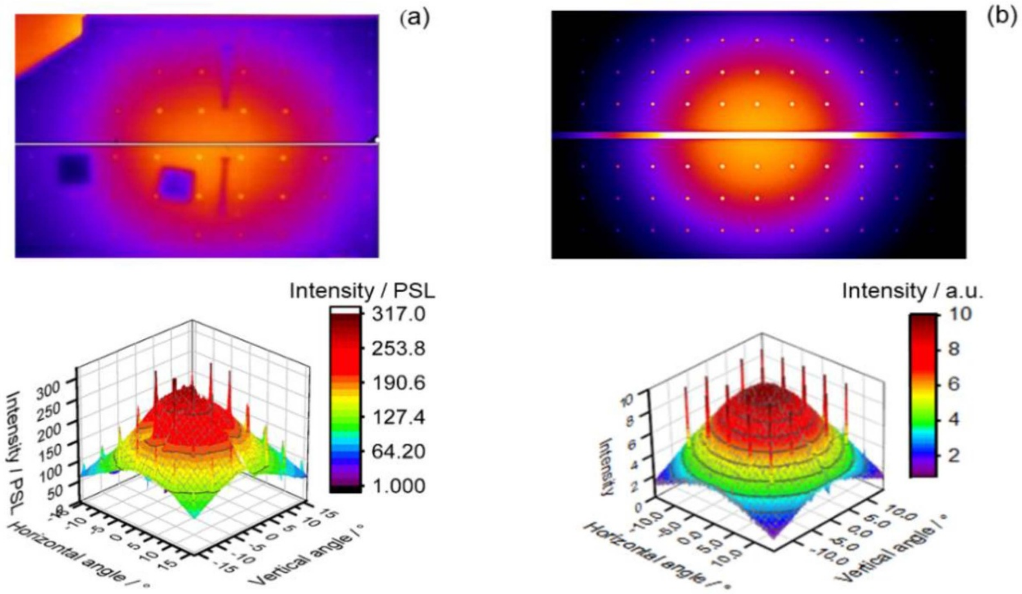

Figure 3. Comparison of the (a) IP image obtained in experiments using the cylinder-stack and (b) GEANT4 simulation result. 'Needles' in the 3D-representation of the image are caused by the holes drilled in the first steel cylinder at a distance of 2 cm from each other to map the electron distribution spatially.

The electron energy distribution measured by three spectrometers placed in the horizontal plane *XOZ* at 0°, 15° and 45° to the laser axis (figure 1(a)) is shown in (figure 4). The shot was made at 1.5 × 10^{19} Wcm^{-2} laser intensity onto a 325 μm thick foam layer pre-ionized by the ns pulse.

One can see that the majority of electrons is accelerated along the laser axis (0°). The measured electron spectra were approximated by a Maxwellian-like distribution functions with one or two temperatures. The electron energy distribution measured at 0° was approximated by one effective temperature $T_1 = 12.0 \pm 1.4$ MeV. The temperature and the number of accelerated electrons drops down to $T_1 \simeq 8.0$ MeV ($T_2 \simeq 11.0$ MeV) at 15° and further to $T_1 \simeq 0.9$ MeV ($T_2 \simeq 2.9$ MeV) at 45°.

For the first time, we explored advantages of a combination of foam layers with thin metallic foils in shots at $\sim 10^{19}$ Wcm^{-2} laser intensity and demonstrated very stable electron signals up to 100 MeV energies. Spectra measured at 0°, 15° and 45° in the interaction of the 1.9 × 10^{19} Wcm^{-2} laser pulse with the foam layer stacked together with a 10 μm thin Au-foil (figures 2(b) and 5) show a strong angular

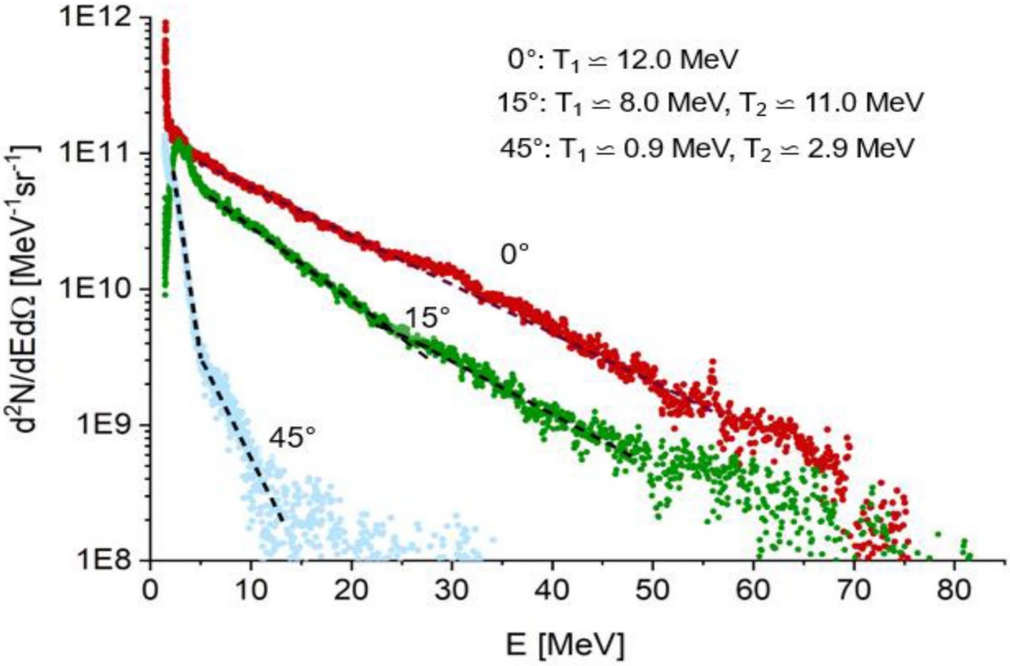

Figure 4. Energy spectra of electrons per steradian measured at 0°(red), 15°(green) and 45°(blue) to the laser propagation direction for a shot onto the pre-ionized foam layer at 1.9×10^{19} Wcm^{-2} laser intensity.

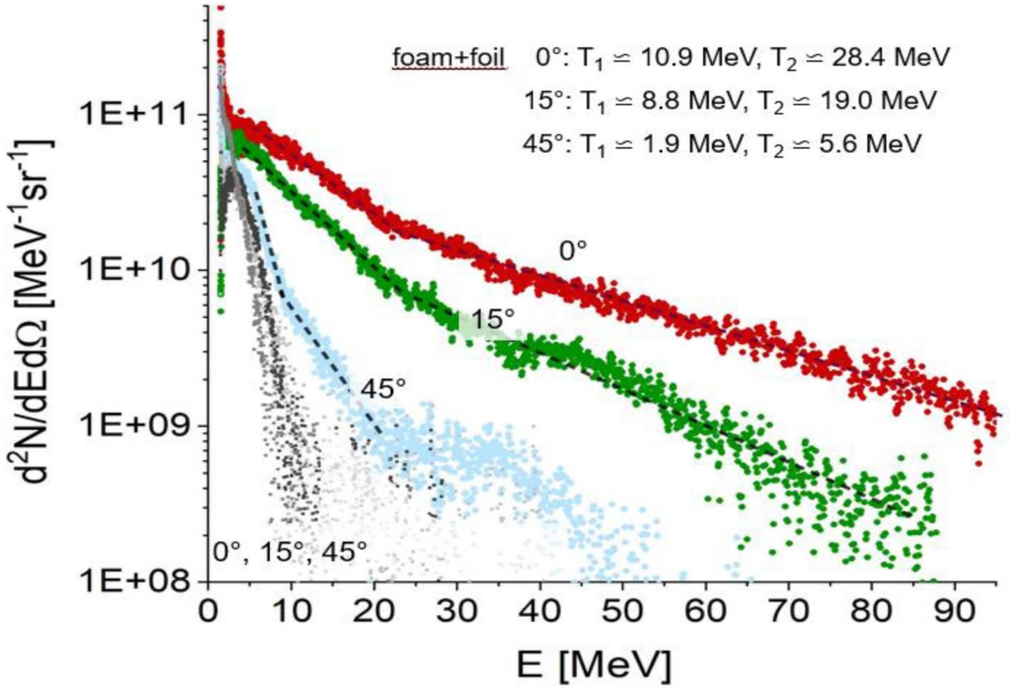

Figure 5. Electron spectra measured at 0°(red), 15°(green) and 45°(blue) to the laser pulse axis for shots at $\sim 10^{19}$ Wcm^{-2} laser intensity. Shots were made onto the pre-ionized foam layer combined with 10 μm Au-foil and directly onto the foil (gray).

dependence similar to that in (figure 4). Additionally, one observes high energy ($E > 25$ MeV) electron tails at 0° and 15° that can be described by an exponential function with a very high second effective temperature of $T_2 = 28.0 \pm 3.4$ MeV for 0° and $T_2 = 19.1 \pm 2.3$ MeV for 15°.

The length of NCD-plasma plays a crucial role in the electron energy gain. Despite moderate relativistic laser intensity, the effective electron temperature measured in our experiment is three times higher than those measured in the interaction of 2×10^{20} Wcm^{-2} laser intensity with double

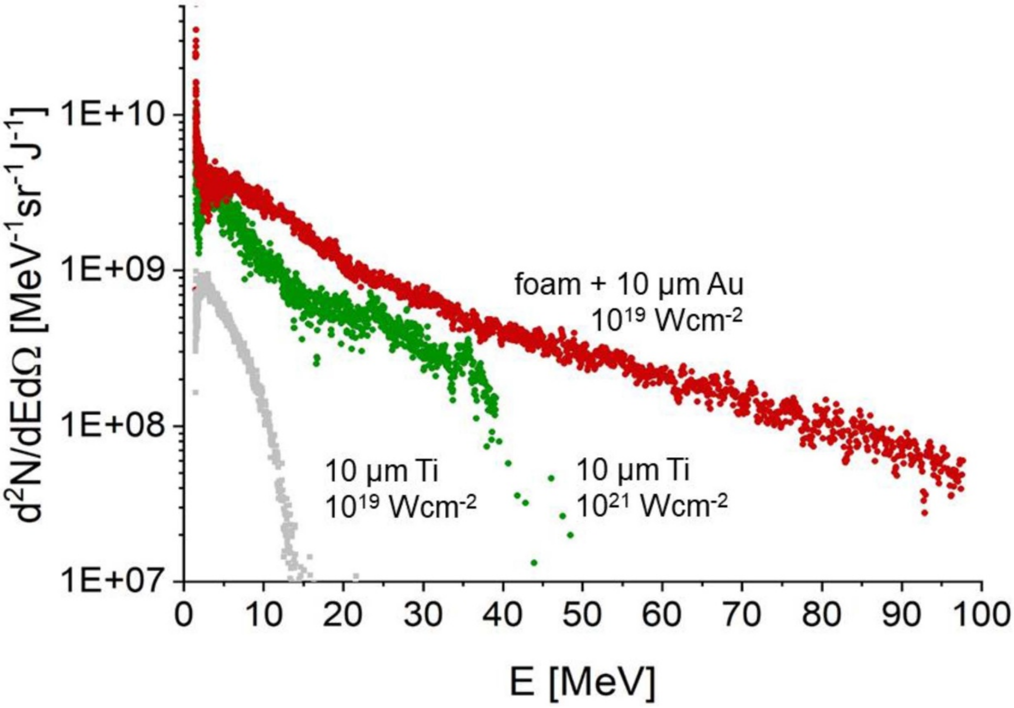

Figure 6. Electron energy distributions are normalized to the corresponding laser energies inside FWHM of the focal spot in Joules. Shots were made onto the pre-ionized low-density foam layer in combination with 10 μm Au-foil at 1.5×10^{19} Wcm^{-2} laser intensity (red) and onto 10 µm thin Ti-foils irradiated by the 9×10^{20} Wcm^{-2} (green) and 1.6×10^{19} Wcm^{-2} (gray) laser intensities. In all cases, spectra were measured along the laser axis (0°).

layered targets, which consist of an NCD slab and an overdense foil [54]. A major reason for this effect is a long acceleration path provided by a 300 μm thick foam layer, while the length of the NCD-plasma in [54] was of several μm only.

In contrast to foams, shots onto 10 μm Ti- or Au-foils at $\sim 10^{19}$ Wcm^{-2} laser intensity shows a near isotropic angular distribution with effective temperatures between 1.4 ± 0.1 MeV (45°) and 2.2 ± 0.2 MeV (0°) (gray signal in figures 5 and 6).

In this experimental campaign, the electron energy distribution was also measured in the interaction of ultra-relativistic laser pulses of 10^{21} Wcm^{-2} intensity (figure 1(b)) with metallic foils. Figure 6 shows the electron signals measured at 0° in the shot made onto the pre-ionized low density foam layer in combination with 10 μm Au-foil at 1.5×10^{19} Wcm^{-2} laser intensity (red) and onto 10 μm thin Ti-foils irradiated at 9×10^{20} Wcm^{-2} (green) and 1.6×10^{19} Wcm^{-2} (gray) laser intensities. The number of accelerated electrons presented in (figure 6) is normalized to the laser energy contained in the FWHM of the focal spot, since in the case of the short focusing parabolic mirror this energy was twice higher than in the long-focus case (36–40 J vs. 17–20 J). The effective temperature of the major fraction of electrons in the case of the ultra-relativistic laser intensity is estimated as high as 6.7 ± 1.2 MeV, which is lower than for shots onto pre-ionized foams at 10^{19} Wcm^{-2} (11–12 MeV). Another important difference can be observed analyzing the maximum of the measured electron energy. In contrast to shots with the ultra-relativistic laser intensity, where the maximum of the measured electron energy does not exceed 40 MeV, the electron spectra, measured at 0° by irradiation of foams in combination with thin foils, show a very stable signal up to 90–100 MeV electron energy (figures 5 and 6).

Once the optimal parameters for the ns-pulse that drives the super-sonic ionization inside the foam were found, the DLA mechanism in the relativistic plasma channel reaches a high level of reproducibility. In measurements at 0°, the effective temperature of the main fraction of super-ponderomotive electrons, averaged over 10 shots onto the pre-ionized foam layers only and onto the combination of foams and foils, reaches 11.5 ± 2.0 MeV.

Figure 7 summarizes data on the number of electrons in different energy ranges and the maximum of the measured electron energy for selected shots made onto various targets irradiated at two laser intensities: $(1.5–1.9) \times 10^{19}$ Wcm^{-2} (blue) and 9.0×10^{20} Wcm^{-2} (red-dashed) and measured at 0°, 15° and 45°. Data is normalized to laser energy in the selected shot. The experimental error of ~25% that occurs by the evaluation of the electron number is caused mostly by the uncertainty of the IP response to the electron impact. This uncertainty remains constant for all electron energies above 0.1 MeV [48]. Additionally, the IP signal fading [49] was taken into account. In the experiment, the IPs were scanned firstly 30–50 min after each laser shot, so that for the signal corrections, a fading factor of 0.65–0.7 was used.

The full height of the bars in (figure 7) corresponds to the total amount of electrons with energies $E > 2$ MeV in steradian normalized to the laser energy contained in the FWHM of the focal spot. For laser intensities of $(1–2.5) \times 10^{19}$ Wcm^{-2} this

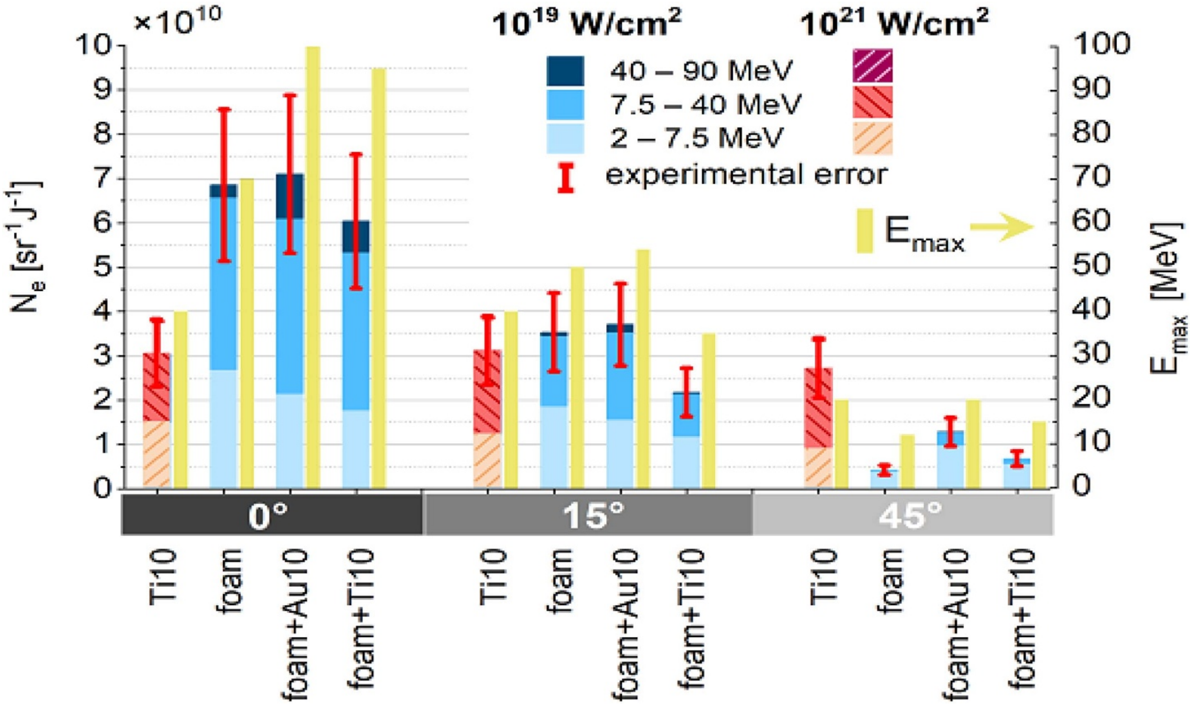

Figure 7. Number of electrons N_e per steradian and per J laser energy for different electron energy ranges for selected shots onto various target types irradiated at two laser intensities: $1.5 \div 1.9 \times 10^{19}$ Wcm^{-2} (blue) and 9×10^{20} Wcm^{-2} (red, dashed) and measured at 0°, 15° and 45°. The maximum of the measured electron energy E_{max} is also shown.

energy was of (17–22) J, while for ultra-relativistic intensity of 10^{21} Wcm^{-2} it reached (36–40) J. The discussed uncertainty in the electron number caused by the IP response is valid in every energy range presented in (figure 7). In the diagram, this uncertainty is shown for the total number of electrons. In the case of the foam target, one counts 7×10^{10} sr^{-1} J^{-1} electrons with E > 2 MeV and 4.4×10^{10} sr^{-1} J^{-1} electrons with E > 7.5 MeV. In the case of the foam layer stacked together with the Au-foil, the total number of electrons with E > 2 MeV is close to the foam-case, while the number of electrons with E > 7.5 MeV is slightly higher and reaches the value of 5.0×10^{10} sr^{-1} J^{-1}. The darkest colored part represents electrons with E > 40 MeV with the highest number obtained in the case of the combination of the foam layer with the 10 μm thin Au-foil. This part of the electron spectrum is of interest e.g. in respect to $(\gamma, x\mathrm{n})$ reactions with tens of MeV threshold gamma-energy.

In results obtained at relativistic laser intensity of 9×10^{20} Wcm^{-2} in the shot onto Ti-foil this part is missing. Although the role of the thin foils in the combination with foams demands further theoretical and experimental investigations, their positive effect is clearly seen by comparing the values of the measured maximum electron energy. In the cases of 'foam + Ti' and 'foam + Au' (figure 7) they lay between 95 and 100 MeV, instead of 70 MeV for the case of foam only.

4. PIC-simulations

3D PIC simulations of the laser propagation in the NCD plasma were performed using the Virtual Laser Plasma Laboratory (VLPL) code [55] for the laser parameters and interaction geometry used in the experiment. In particular, the laser pulse intensity in time and space was approximated by a Gaussian distribution. Elliptical form of the focal spot was taken from the experiment with FWHM axes 11 μm in a vertical and 15 μm a horizontal direction. The laser pulse energy in the FWHM focal spot of 17.5 J and the FWHM pulse length of 700 fs resulted into the laser intensity of 2.5×10^{19} Wcm^{-2} with $a_L = 4.28$. The homogeneous plasma was composed of electrons and fully ionized ions of carbon, hydrogen and oxygen. Simulations accounted for the ion type and the ion fraction in accordance with the chemical composition of triacetate cellulose $C_{12}H_{16}O_8$, see e.g. [46, 47]. The simulation box had sizes of $350 \times 75 \times 75$ μm^3. The first 10 and the last 15 μm from the total 350 μm of the space in x-direction (the laser axis) were free of the plasma initially. Sizes of a numerical cell were 0.1 μm along the x-axis and 0.5 µm along the y-axis and the z-axis. The number of particles per cell in the simulation was 4 for the electrons and 1 for the ions of each type. Boundary conditions were absorbing for particles and fields in each direction.

The initial electron density (together with the neutralizing ion density) at the moment of the main pulse arrival was of 0.65 n_{cr} with a step-like profile. Previously, PIC-simulations were performed for a step-like density profile with n_{cr} and 0.5 n_{cr} [40, 41] and for a partially ramped density profile in order to account for plasma expansion toward the main laser pulse [43]. The simulations result in a very similar overall behavior of the energy and angular distributions of super-ponderomotive electrons in all mentioned cases.

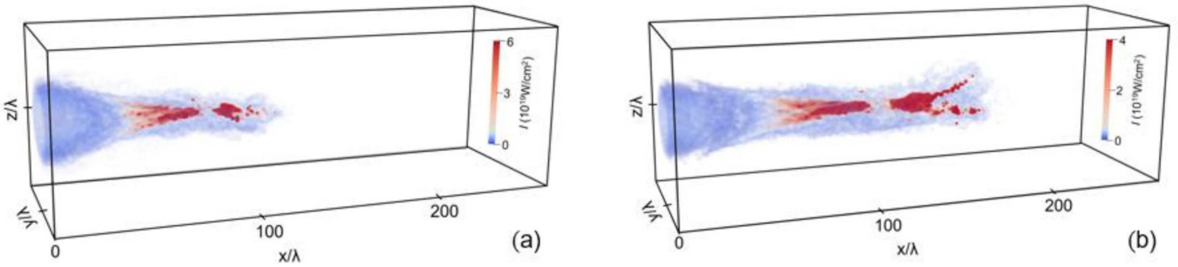

Figure 8. 3D view of the laser intensity distribution at time moments $t_1 = 100$ fs (a) and $t_2 = 433$ fs (b). The time $t = 0$ corresponds to the maximum laser pulse intensity on the target front side (x = 10 μm).

Figure 8 gives a 3D view of the laser intensity by propagation of the laser pulse in the NCD plasma at time moments $t_1 = 100$ fs (a) and $t_2 = 433$ fs (b).

The laser pulse propagates from the left to right and at $t = 0$ its maximum intensity is on the target front side ($x = 10\ \mu$m). We observe strong self-focusing (a) and later filamentation (b) of the laser pulse that produces the main channel and, at the end of interaction, a few side channels inside the plasma. For the discussed moderate laser energy (~20 J), the filamentation of the laser pulse takes place only by the end of the acceleration process (at $t_2 = 433$ fs, figure 8(b)). In this case, the main fraction of accelerated electrons already gained the energy in the filament-free part of the channel and the laser filamentation weekly effects the energy gain and the angular distribution of the electron beam. With an increased laser energy, filamentation starts to be much more pronounced and occurs at earlier times [40]. It manifests itself in the filamentation of the current of accelerated electrons and in the worse collimation of the generated electron beams. Nevertheless, simulations show that the DLA process continues to be very effective [40].

The laser ponderomotive force expels background plasma electrons off the channel and creates a radial quasi-static electric field. At the same time, the current of the accelerated relativistic electrons generates an azimuthal magnetic field. The structure of the quasi-static self-generated E and B-fields was analyzed in detail in [32–35] and in publications that consider PHELIX-laser parameters [40, 43]. In [43] it is shown that the electron current density in the relativistic plasma channel reaches 10^{11} A cm^{-2} and the quasi-static azimuthal magnetic field exceeds 100 MG.

Figure 9 presents snapshots of the electron phase space 100 fs after the laser pulse peak intensity arrived at the left plasma boundary. Acceleration occurs mostly in the laser pulse propagation direction x, as it can be seen in (figure 9(a)), where the electron momentum p_x grows approaching ~100 mc. The high values of the transversal electron momentum $p_y \sim 30$–$50\ mc$ (laser polarization direction) (figure 9(b)) and $p_z \sim 20\ mc$ (figure 9(c)) are much larger than the normalized amplitude of the laser pulse $a_0 = eE_0/mc\omega \sim 5$. These large values of the electron transverse momenta are due to the resonance between the electron betatron frequency in the channel fields and the Doppler shifted laser frequency [32, 33]. Then, magnetic field converts the gained transverse particle momentum into the longitudinal one via the v x B force. Figure 9(d) zooms the p_y vs x electron phase space in the range [43–70] x/λ, where we clearly see that the electron transverse oscillations are modulated at the laser phase.

In the PIC simulation, we registered electrons leaving the NCD plasma. Angular distribution of the electrons with $E > 7.5$ MeV is shown in (figure 10) in spherical coordinates with a polar axis OX along the laser propagation direction: $\theta = \arctan(\sqrt{p_y^2 + p_z^2}/p_x)$, $\varphi = \arctan(p_z/p_y)$. One can see that a high fraction of the super-ponderomotive electrons is accelerated in the laser direction and propagate in the rather tight divergence cone with a half angle of 10°-12°. This result supports the experimental measurements presented in (figure 3).

The 3D capability of the PIC code allows for simulations close to the real experimental conditions. Thus, the absolute energy spectra, i.e. the number of accelerated electrons in any energy range and their angular distribution can be obtained.

The electron spectra presented in (figure 11) were simulated in the horizontal plane for $\theta = 0° \pm 2°$ (red dots), $15° \pm 2°$(green dots) and $45° \pm 2°$ (blue dots), which correspond to the positions of the electron spectrometers in the experiment (figure 1(a)). The obtained effective temperatures are in good agreement with the experimental results presented in (figure 4) for all three observation directions. According to simulations, the total number of electrons with E > 2 MeV, propagating in 2π, reaches the value of 5×10^{12} that corresponds to ~ 1 μC of the electron charge and 27% conversion of the laser energy into relativistic electrons. Current simulations show that only 12% of electrons with E > 2 MeV are contained in the 0.16 sr divergence cone. Another situation is with the super-ponderomotive electrons with energies beyond 7.5 MeV that are relevant for gamma-driven nuclear reactions. Simulations result into $N_e = 3.3 \times 10^{11}$ electrons contained in 0.16 sr, that is 30% of all super-ponderomotive electrons with E > 7.5 MeV propagating in 2π. This number is in good agreement with the experimental value of $(2 \pm 0.6) \times 10^{11}$.

Based on the results of simulations and measurements, one can estimate a charge carried by the super-ponderomotive electrons with E > 2 MeV and E > 7.5 MeV propagating along the laser axis inside the divergence cone of 0.16 sr as high as ~100 and ~50 nC with corresponding conversion efficiencies of 12% and 6%.

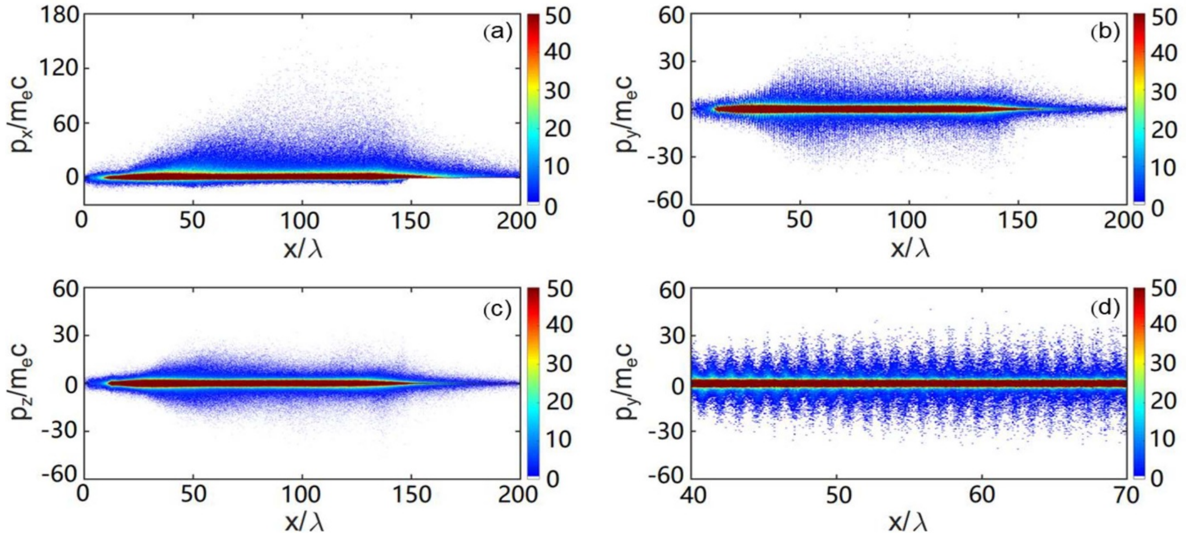

Figure 9. Snapshots of the electron phase space 100 fs after the laser pulse peak intensity arrived at the left plasma boundary: (a) momentum p_x vs x; (b) momentum p_y vs x; (c) momentum p_z vs x; (d) zoomed part of momentum p_y vs x in the range $x/\lambda = [43, 70]$. Color panels present a number of pseudo-electrons in simulations.

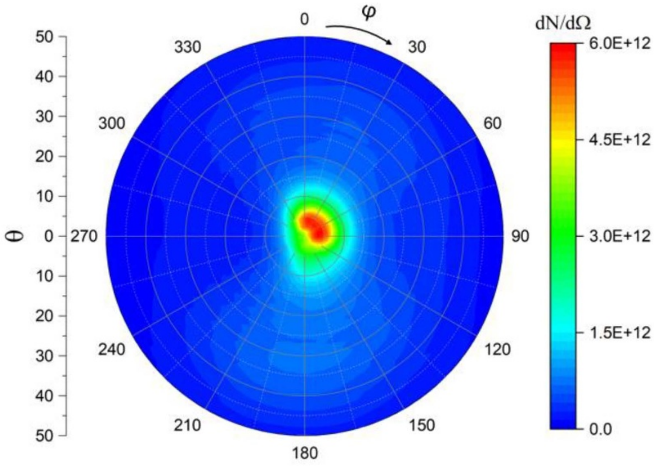

Figure 10. Angular distributions of electrons $dN/d\Omega$ [sr^{-1}] with energies E > 7.5 MeV that left the simulation box by the time $t = 2.5$ ps.

5. Gamma-ray generation

High-current and well-directed electron beams with energies of several tens of MeV are excellently suited for the production of ultra-intense gamma sources by penetration of high Z materials.

In our experiment, the MeV bremsstrahlung spectrum was evaluated from the yields of gamma-induced nuclear reactions as it was done in [52]. For this purpose, 1 mm-thick activation samples of Au, Ta, Cr and 0.25 mm thin In-foil of 15 × 15 mm^2 area were placed at 6° ± 1° and 16° ± 1° to the laser pulse propagation direction 150–230 mm away from the target position (figures 2(c) and (d)). The shot at 1.5 × 10^{19} Wcm^{-2} laser intensity was made onto the pre-ionized foam layer stacked together with 1 mm thick Au-plate. After irradiation by electrons and gammas, all activation samples were counted multiple times on a low background HPGe-detector to identify nuclides via known γ-ray energies, intensities, and half-life times. High reaction yields of the isotopes $^{196\,194,192}$Au, ^{180,178m}Ta and ^{51,49}Cr measured in the activation samples at 5° to the laser axis are shown in (figure 12). The isotope yields measured in the samples placed at 15° to the laser axis were at least one order of magnitude lower.

The normalization of the experimental data presented in (figure 12) was made by taking the laser energy in the FWHM of the laser focal spot (20 J in case of 10^{19} Wcm^{-2} and 40 J in the case of 10^{21} Wcm^{-2} laser intensities) and a solid angle of 7 × 10^{-3} sr covered by the activation samples into account. For determination of the reaction yield, the efficiency of the HPGe-detector, the intensities of γ-lines and the detector dead time were taken into consideration. The uncertainty in the reaction yields is mainly due to the uncertainty in the number of counts in the full energy peaks. Dark blue colored bars in (figure 12) show the reaction yields obtained in the shot at 1.5 × 10^{19} Wcm^{-2} laser intensity onto a pre-ionized foam layer stacked together with 1 mm thick Au-plate. The reaction yields for 10^{21} Wcm^{-2} laser intensity are presented by light sand colored bars. In shots at (1–2) × 10^{19} Wcm^{-2} laser intensity, we observe up to 50-times higher ^{194}Au isotopes yields with the threshold gamma energy $E\gamma \simeq 22$ F-23 MeV compared to the laser shots directly onto the convertor plate at 10^{21} Wcm^{-2}. The ^{192}Au isotopes created in (γ, 5n) reactions with the cross-section threshold at $E_\gamma \simeq 38.7$ MeV were observed in shots onto pre-ionized foams at ∼10^{19} Wcm^{-2} only. The substantial difference in the isotope production yield for these two cases of the laser-matter interaction can be explained by the difference in the measured electron spectra shown in (figures 5 and 6).

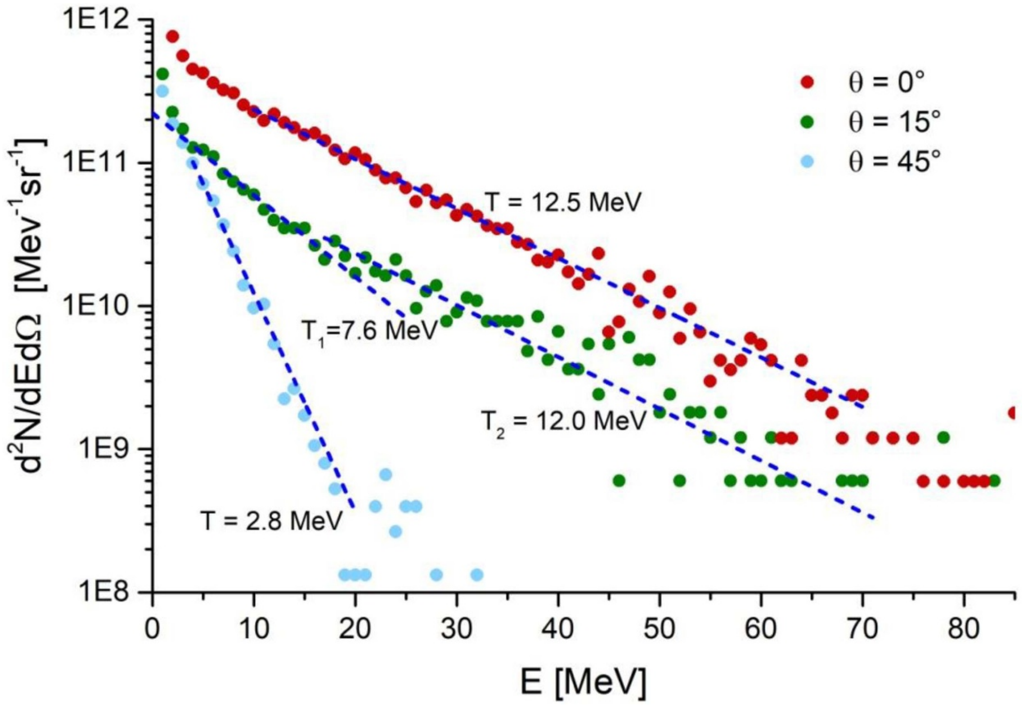

Figure 11. Energy distributions of electrons per steradian ($d^2N/dEd\Omega$) that leave the simulation box at $t = 2.5$ ps for three different angles $\theta = 0°$(red), 15°(green) and 45°(blue) in the horizontal plane *XOZ*.

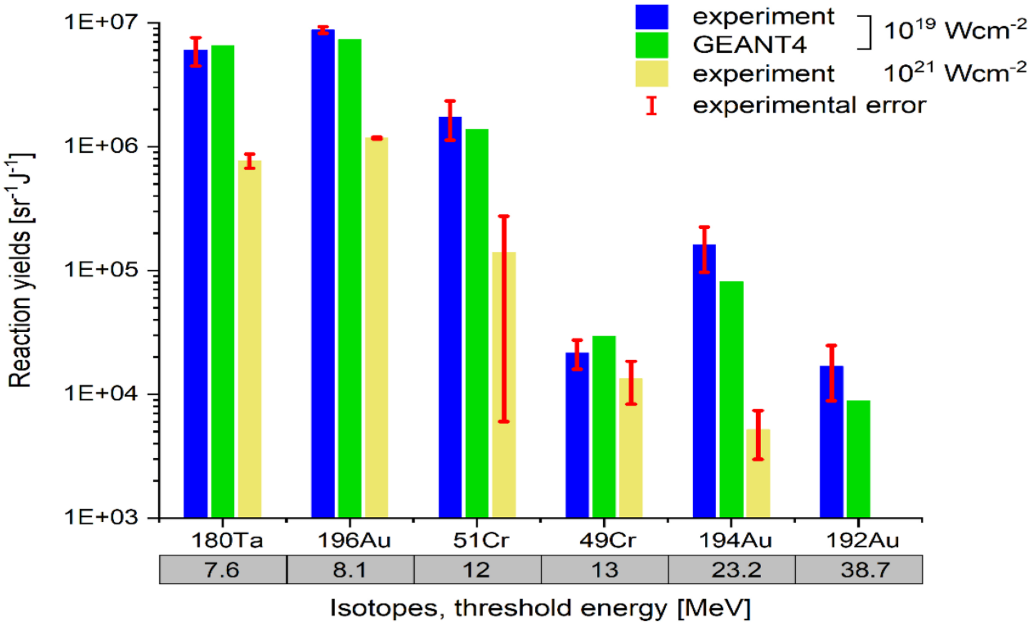

Figure 12. Experimental data on (γ, xn) reaction yields in Au, Ta und Cr and results of GEANT4 simulations normalized to steradian and the laser energy in the corresponding shot. Blue colored bars present reaction yields obtained in the shot at 1.5×10^{19} Wcm^{-2} laser intensity onto a pre-ionized foam layer stacked together with 1 mm thick Au-plate used as a radiator. Green bars show reaction yields simulated for this case with GEANT 4. The reaction yields measured in the shot at 10^{21} Wcm^{-2} directly onto the radiator plate is shown by light sand colored bars. In the gray row below the figure, the threshold photon energies for the production of the corresponding isotope are presented.

The bremsstrahlung spectra reconstructed from the measured Au, Ta and Cr isotopes yields were described by an exponential function with an effective temperature of 12.7 ± 2.4 MeV for the laser shot at 1.5×10^{19} Wcm^{-2} intensity and 5.4 ± 1.7 MeV in the case of the laser shot at 10^{21} Wcm^{-2}. Interaction of the super-ponderomotive electrons with high-Z samples resulted in a gamma fluence N_γ (>7.5 MeV) $= 2.0 \pm 0.5 \times 10^9$ cm^{-2} at 180 mm distance. This is 10-times higher than the value obtained in the laser shot at ultra-relativistic laser intensity.

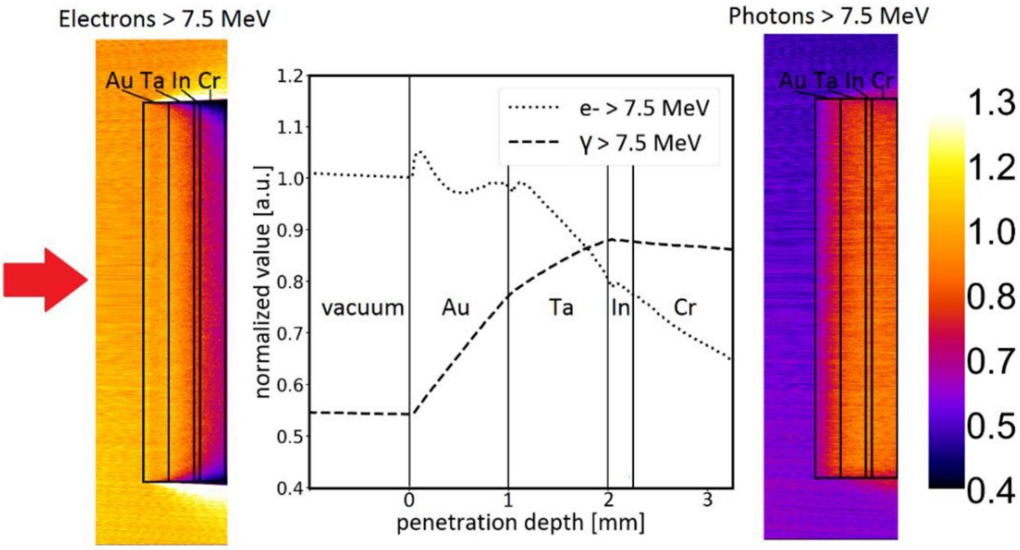

Figure 13. Electron and gamma fluencies (E > 7.5 MeV) in arbitrary units in dependence on the penetration depth in the stack of activation samples Au/Ta/In/Cr.

Table 1. Number of MeV-photons N_{ph} and effective temperature T_{eff} of the bremsstrahlung spectrum generated by super-ponderomotive electrons in 1 cm × 1 cm × 0.5 cm Au-block in dependence on the penetration depth.

Au-radiator thickness Energy range	0.1 mm		1 mm		3 mm		5 mm	
	$T_{eff,\ MeV}$	N_{ph}	$T_{eff,\ MeV}$	N_{ph}	$T_{eff,\ MeV}$	N_{ph}	$T_{eff,\ MeV}$	N_{ph}
1–7 MeV	2.5	5×10^{10}	2.5	2×10^{11}	2.5	7×10^{11}	2.5	6×10^{11}
7–70 MeV	6.1–11.4	6×10^{10}	5.9–10.7	1×10^{11}	5.7–9.8	2×10^{11}	5.6–9.3	1.6×10^{11}

The modeling of the electron beam interaction with the activation samples was performed by means of the GEANT4 Monte Carlo code [56–58] for the discussed experimental geometry. Green bars in (figure 12) show simulated reaction yields that are in a good agreement with the experiment. In the modeling, the measured electron energy distribution together with the divergence angle of super-ponderomotive electrons were used as input parameters. The activation samples of Ta, Au, In and Cr were 'placed' at 5° to the laser axis 180 mm away from the laser-foam interaction point. The electron beam traversed the 1 mm Au-radiator producing MeV-bremsstrahlung. The high fraction of the relativistic electrons that escape the radiator together with gamma-radiation propagated in vacuum and interacted with the activation samples.

For the simulations, cross sections for (γ, xn) reactions in Au, Ta and Cr were taken from [56]. A cross check between these cross sections and those from [59] used for the reconstruction of the gamma-spectrum from experimentally measured isotope yields provided a good agreement. Figure 12 shows the transformation of the relativistic electrons with E > 7.5 MeV, which heat the Au-activation sample from the left side at first, into gamma-rays in dependence on the penetration depth in the stack. Vertical cross sections in (figure 13) made through the central part of the stack show a normalized electron (left panel) and a photon (right panel) fluence. The initial level of the bremsstrahlung radiation of 0.55 a.u. that heats the stack is generated by the super-ponderomotive electrons in the 1 mm thick Au-radiator, an additional gamma-fluence of $\geq$0.3 a.u. was produced by the relativistic electrons in the activation samples. A slight increase of the electron number in the Au-vacuum interface is caused by gamma-rays.

The simulations result in the bremsstrahlung radiation with effective temperatures of $T_1 \simeq 7.1$ MeV ($E_\gamma = 10$–20 MeV) and $T_2 \simeq 11.2$ MeV ($E_\gamma = 25$–60 MeV). A peak photon number of 1.6×10^9 cm^{-2} was reached after electron propagation in the 1 mm-thick Au-radiator and 2 mm in the activation samples. These values are in a good agreement with the experimental results. We would like to note that the above mentioned ultra-high gamma fluence was generated in the samples situated 180 mm away from the laser-foam interaction point. The solid angle covered by the activation stack with 2.25 cm^2 area is 7×10^{-3} sr. This means that $\leq$4% of the MeV gamma-rays and the super-ponderomotive electrons generated at the target position participated in the gamma-ray production.

GEANT-4 simulations were performed for an optimized set-up geometry. In simulations, a 1 cm × 1 cm × 0.5 cm Au-block was placed at 1 cm distance from the NCD-target and irradiated by the beam of super-ponderomotive electrons (figure 5, 0°). In this geometry, 100% of multi-MeV electrons participate in the MeV-bremsstrahlung generation. Table 1 shows the number of MeV-photons N_{ph} and effective temperature T_{eff} of the bremsstrahlung spectrum in dependence on the photon energy range and the depth in the Au-block. The highest photon number with energies 1–70 MeV is obtained at 3 mm of the Au-depth and reaches $\sim 10^{12}$ photons. Simulations show that the gamma-beam is directed along the laser axis within a divergence cone of 0.4 sr. The increase of the MeV-photon number with the target thickness can be explained with a long collision free path of multi-MeV-electrons in the target. At a higher thickness (e.g. at 5 mm) the photon attenuation caused by the Compton scattering and the pair production starts to play a role and the photon number drops slightly. The effective temperatures of the bremsstrahlung radiation for two photon energy regions presented in table 1 reflect the two-temperature distribution of the primary electron beam (figure 5). The yields of gamma-driven nuclear reactions follow the gamma-fluence trend.

Summarizing the results presented in table 1, one can conclude that interaction of high-current well-directed relativistic electrons with high Z targets leads to effective production of MeV bremsstrahlung radiation with the ultra-high fluence of $\sim 10^{12}$ cm^{-2} and the flux of $\sim 10^{23}$ cm^{-2} s^{-1} assuming a 10 ps gamma-ray pulse in the case of 3 mm target thickness. The conversion efficiency of the laser energy into the energy of gammas beyond >1 MeV reaches 1.5%, while for the region of the giant dipole resonance (GDR) with photon energies $E > 7$ MeV it is of 0.8%.

6. Summary

The experimental results and numerical simulations demonstrate an extremely high capability of the well-directed high-current relativistic electron beams to be used in novel laser assisted applications exploiting already existing high-energy sub-PW and PW-class laser systems. This makes our approach crucial for applications promising a strong enhancement of the characteristics of the laser driven sources of particles and photons.

In the reported experiment, ultra-relativistic electron beams were produced in the interaction of $\sim 10^{19}$ Wcm^{-2} laser pulses with plasmas of near critical electron density by the mechanism of direct laser acceleration (DLA). We investigated the angular dependence of the electron acceleration process and measured the high effective electron temperature of 10–13 MeV and the maximum of the electron energy of 100 MeV in the laser pulse propagation direction. A high stability and reproducibility of the acceleration process was observed. The laser energy conversion efficiency into electrons with energies above 2 MeV reached 23% with a total charge approaching 1 μC.

For application purposes, we analyzed the charge carried by the super-ponderomotive electrons propagating with $E > 7.5$ MeV. Counting only for electrons in 0.16 sr divergence cone, it reaches $\sim$50 nC with the corresponding laser conversion efficiency of $\sim$6%. These results are supported by the full 3D PIC-simulations.

The measured effective electron temperature and the maximum of the electron energy were twice higher for shots onto pre-ionized foams at $\sim 10^{19}$ Wcm^{-2} than for direct laser shots onto standard foils at ultra-relativistic laser intensity of $\sim 10^{21}$ Wcm^{-2}. The substantial difference in the electron spectra for these two cases presented itself in the isotope production yield. We detected high yield nuclear reactions demanding tens of MeV gamma-rays in shots onto pre-ionized foam layers and their combination with foils.

The interaction of the super-ponderomotive electrons with high-Z samples, placed 180 mm away from the target position, resulted in the photon fluence in the GDR-region of $(2.0 \pm 0.5) \times 10^{9}$ cm^{-2} with 12.7 ± 2.4 MeV effective temperature. For the optimized target set-up geometry, we obtain an ultra-high MeV photon number of $\sim 10^{12}$. The gamma-beam is directed along the laser axis within a divergence cone of 0.4 sr. For the gamma-ray energies beyond 7 MeV, the optimization of the target set-up results in 2×10^{11} photons per laser shot and a corresponding fluence of 2×10^{11} cm^{-2}. The effective temperature of the bremsstrahlung spectrum is up to 10 MeV and a corresponding laser-to-gamma conversion efficiency of 0.8% obtained at $\sim 10^{19}$ Wcm^{-2} laser intensity.

Ultra-intense well-directed beams of MeV electrons and gamma-rays discussed in our paper were obtained at laser intensities that are relevant for the current short pulse high energy diagnostic lasers e.g. at NIF and LMJ. Application of the low-density polymer foams will result in a strong increase of their diagnostic potential in probing of high energy density matter.

Acknowledgments

The results presented here are based on the experiment P176, which was performed at the PHELIX facility at the GSI Helmholtzzentrum fuer Schwerionenforschung, Darmstadt (Germany) in the frame of FAIR Phase-0. The experimental group is very thankful for the support provided by the PHELIX-laser team at GSI-Darmstadt. We thank also Dr B. Borm for the development of the electron spectrometers. The research leading to these results has received funding from LASERLAB-EUROPE (grant agreement no. 654148, European Union's Horizon 2020 research and innovation program). This work was also funded by the Grant Nos. 16 APPA (GSI) of the Ministry of Science and Higher Education of the Russian Federation, by the Project DFG PU 213/9-1, the RFBR project 19-02-00875, the RFBR and ROSATOM project 20-21-00150, and within the framework of the EUROfusion Consortium by the Euroatom research and training programs 2014−2018 and 2019–2020 under the grant agreement No. 633053. The views and opinions expressed herein do not necessarily reflect those of the European Commission.

ORCID iDs

O N Rosmej https://orcid.org/0000-0003-0447-3510
F Consoli https://orcid.org/0000-0001-8694-3357

References

[1] Wang T, Ribeyre X, Gong Z, Jansen O, d'Humières E, Stutman D, Toncian T and Arefiev A 2020 Power scaling for collimated g-ray beams generated by structured laser-irradiated targets and its application to two-photon pair production *Phys. Rev. Appl.* **13** 054024

[2] Norreys P A *et al* 1999 Observation of a highly directional g-ray beam from ultrashort, ultraintense laser pulse interactions with solid *Phys. Plasmas* **6** 2150

[3] Hatchet S P *et al* 2000 Electron, photon, and ion beams from the relativistic interaction of Petawatt laser pulses with solid targets *Phys. Plasmas* **7** 2076

[4] Zhu X L, Chen M, Weng S-M, Yu T-P, Wang W-M, He F, Sheng Z-M, McKenna P, Jaroszynski D A and Zhang J 2020 Extremely brilliant GeV g-rays from a two-stage laser-plasma accelerator *Sci. Adv.* **6** eaaz7240

[5] Gu Y, Jirka M, Klimo O and Weber S 2019 Gamma photons and electron-positron pairs from ultra-intense laser-matter interaction: A comparative study of proposed configurations *Matter Radiat. Extremes* **4** 064403

[6] Zhu X L, Yu T-P, Sheng Z-M, Yin Y, Turcu I C E and Pukhov A 2016 Dense GeV electron-positron pairs generated by laser in near–critical density plasmas *Nat. Commun.* **7** 13686

[7] Ridgers C P *et al* 2012 Dense electron-positron plasma and ultraintense g-rays from laser –irradiated solids *Phys. Rev. Lett.* **108** 165006

[8] Pomerantz I *et al* 2014 Ultrashort pulsed neutron source *Phys. Rev. Lett.* **113** 184801

[9] Kampfrath T, Tanaka K and Nelson K A 2013 Resonant and nonresonant control over matter and light by intense terahertz transients *Nat. Photonics* **7** 680

[10] Koenig S *et al* 2013 Wireless sub-THz communication system with high data rate *Nat. Photonics* **7** 977

[11] Herzer S *et al* 2018 An investigation on THz yield from laser-produced solid density plasmas at relativistic laser intensities *New J. Phys.* **20** 063019

[12] Kostyukov I, Kiselev S and Pukhov A 2003 X-ray generation in an ion channel *Phys. Plasmas* **10** 4818–28

[13] Kislev S, Pukhov A and Kostyukov I 2004 X-ray generation in strongly nonlinear plasma wave *Phys. Rev. Lett.* **93** 135004

[14] Rousse A *et al* 2004 Production of a keV X-ray beam from synchrotron radiation in relativistic laser-plasma interaction *Phys. Rev. Lett.* **93** 135004

[15] Cipiccia S *et al* 2011 Gamma-rays from harmonically resonant betatron oscillation in plasma wake *Nat. Phys. Lett.* **7** 867–71

[16] Albert F *et al* 2017 Observation of betatron x-ray radiation in a self-modulated laser wakefield accelerator driven with picosecond laser pulses *Phys. Rev. Lett.* **118** 134801

[17] Kneip S *et al* 2008 Observation of synchrotron radiation from electrons accelerated in a petawatt-laser-generated plasma cavity *Phys. Rev. Lett.* **100** 105006

[18] Ravasio A *et al* 2008 Hard x-ray radiography for density measurement in shock compressed matter *Phys. Plasmas* **15** 060701

[19] Li K, Borm B, Hug F, Khaghani D, Löher B, Savran D, Tahir N A and Neumayer P 2014 Developments toward hard X-ray radiography on heavy-ion heated dense plasmas *Laser Part. Beams* **32** 631

[20] Negoita F *et al* 2016 Laser driven nuclear physics at ELI-NP *Rom. Rep. Phys.* **68** 37–144

[21] Habs D and Köster U 2011 Production of medical radioisotopes with high specific activity in photonuclear reactions with γ-beams of high intensity and large brilliance *Appl. Phys. B* **103** 501–19

[22] Ma Z, Lan H, Liu W, Wu S, Xu Y, Zhu Z and Luo W 2019 Photonuclear production of medical isotopes 62,64Cu using intense laser-plasma electron source *Matter Radiat. Extremes* **4** 064401

[23] Esarey E, Schroeder C B and Leemans W P 2009 Physics of laser-driven plasma-based electron accelerators *Rev. Mod. Phys.* **81** 1229

[24] Pukhov A and Meyer-ter-vehn J 2001 Laser wake field acceleration: the highly non-linear broken-wave regime *Appl. Phys.* B **74** 355

[25] Faure J, Glinec Y, Pukhov A, Kiselev S, Gordienko S, Lefebvre E, Rousseau J-P, Burgy F and Malka V 2004 A laser-plasma accelerator producing monoenergetic electron beams *Nature* **431** 541

[26] Mangles S *et al* 2004 Monoenergetic beams of relativistic electrons from intense laser–plasma interactions *Nature* **431** 535

[27] Geddes C G R, Toth C, van Tilborg J, Esarey E, Schroeder C B, Bruhwiler D, Nieter C, Cary J and Leemans W P 2004 High-quality electron beams from a laser wakefield accelerator using plasma-channel guiding *Nature* **431** 538

[28] Gonsalves A J *et al* 2019 Petawatt laser Guiding and electron beam acceleration to 8 GeV in a laser-heated capillary discharge waveguide *Phys. Rev. Lett.* **122** 084801

[29] Huang Z, Ding Y and Schroeder C B 2012 Compact x-ray free-electron laser from a laser-plasma accelerator using a transverse-gradient undulator *Phys. Rev. Lett.* **109** 204801

[30] Maier A R *et al* 2012 Demonstration scheme for a laser-plasma-driven free-electron laser *Phys. Rev.* X **2** 031019

[31] Seggebrock T, Maier A R, Dornmair I and Grüner F 2013 Bunch decompression for laser-plasma driven free-electron laser demonstration schemes *Phys. Rev. Spec. Top. Accel Beams* **16** 070703

[32] Pukhov A, Sheng Z-M and Meyer-ter-vehn J 1999 Particle acceleration in relativistic laser channels *Phys. Plasmas* **6** 2847

[33] Pukhov A 2003 Strong field interaction of laser radiation *Rep. Prog. Phys.* **66** 47–101

[34] Arefiev A V, Khudik V N, Robinson A P L, Shvets G, Willingale L and Schollmeier M 2016 Beyond the ponderomotive limit: direct laser acceleration of relativistic electrons in sub-critical plasmas *Phys. Plasmas* **23** 056704

[35] Willingale L *et al* 2018 The unexpected role of evolving longitudinal electric fields in generating energetic electrons in relativistically transparent plasmas *New J. Phys.* **20** 093024

[36] Bochkarev S G, Brantov A V, Bychenkov V Y, Torshin D V, Kovalev V F, Baidin G V and Lykov V A 2014 Stochastic electron acceleration in plasma waves driven by a high-power subpicosecond laser pulse *Plasma Phys. Rep.* **40** 202–14

[37] Bagnoud V *et al* 2010 Commissioning and early experiments of the PHELIX facility *Appl. Phys.* B **100** 137–50

[38] Gray R J *et al* 2014 Laser pulse propagation and enhanced energy coupling to fast electrons in dense plasma gradient *New J. Phys.* **16** 113075

[39] Willingale L *et al* 2013 Surface waves and electron acceleration from high-power, kilojoule-class laser interaction with underdense plasma *New J. Phys.* **15** 025023

[40] Pugachev L P *et al* 2016 Acceleration of electrons under the action of petawatt-class laser pulses onto foam targets *Nucl. Instrum. Methods Phys. Res.* A **829** 88–93

[41] Pugachev L P and Andreev N E 2019 Characterization of accelerated electrons generated in foams under the action of petawatt lasers *J. Phys.: Conf. Ser.* **1147** 012080

[42] Borisenko N G, Khalenkov A M, Kmetik V, Limpouch J, Merkuliev Y A and Pimenov V G 2007 Plastic aerogel targets and optical transparency of undercritical microheterogeneous plasma *Fusion Sci. Technol.* **51** 655–64

[43] Rosmej O N *et al* 2019 Interaction of relativistically intense laser pulses with long-scale near critical plasmas for optimization of laser based sources of MeV electrons and gamma-rays *New J. Phys.* **21** 043044

[44] Gus'kov S Y, Limpouch J, Nicolaï P and Tikhonchuk V T 2011 Laser-supported ionization wave in under-dense gases and foams *Phys. Plasmas* **18** 103114

[45] Nicolaï P *et al* 2012 Experimental evidence of foam homogenization *Phys. Plasmas* **19** 113105

[46] Khalenkov A M, Borisenko N G, Kondrashov V N, Merkuliev Y A, Limpouch J and Pimenov V G 2006 Experience of micro-heterogeneous target fabrication to study energy transport in plasma near critical density *Laser Part. Beams* **24** 283–90

[47] Borisenko N G *et al* 2006 Regular 3-D networks with clusters for controlled energy transport studies in laser plasma near critical density *Fusion Sci. Technol.* **49** 676–85

[48] Bonnet T, Comet M, Denis-Petit D, Gobet F, Hannachi F, Tarisien M, Versteegen M and Aléonard M M 2013 Response functions of imaging plates to photons, electrons and 4He particles *Rev. Sci. Instr.* **84** 103510

[49] Tanaka K A, Yabuuchi T, Sato T, Kodama R, Kitagawa Y, Takahashi T, Ikeda T, Honda Y and Okuda S 2005 Calibration of imaging plate for high energy electron spectrometer *Rev. Sci. Instr.* **76** 013507

[50] Rusby D R *et al* 2015 Measurement of the angle, temperature and flux of fast electrons emitted from intense laser-solid interactions *J. Plasma Phys.* **81** 475810505

[51] Stoyer M A *et al* 2001 Nuclear diagnostics for petawatt experiments *Rev. Sci. Instr.* **72** 767–72

[52] Günther M M, Sonnabend K, Brambrink E, Vogt K, Bagnoud V, Harres K and Roth M 2011 A novel nuclear pyrometry for the characterization of the high-energy bremsstrahlung and electrons produced in relativistic laser-plasma interactions *Phys. Plasmas* **18** 083102

[53] Zankl G, Strachan J D, Lewis R, Pettus W and Schmotzer J 1981 Neutron flux measurements around the Princeton large tokamak *Nucl. Instrum. Methods Phys. Res.* **185** 321–9

[54] Bin J *et al* 2018 Enhanced laser-driven ion acceleration by superponderomotive electrons generated from near-critical-density plasma *Phys. Rev. Lett.* **120** 074801

[55] Pukhov A 1999 Tree-dimensional electromagnetic relativistic particle-in-cell code VLPL (virtual laser plasma lab) *Plasma Phys.* **61** 425–33

[56] Geant4 Toolkit (available at: http://geant4-userdoc.web.cern.ch/geant4-userdoc/UsersGuides/ForApplicationDeveloper/fo/BookForApplicationDevelopers.pdf)

[57] Geant4 Toolkit, physicslist (available at: http://geant4-userdoc.web.cern.ch/geant4-userdoc/UsersGuides/PhysicsListGuide/fo/PhysicsListGuide.pdf)

[58] GEANT4 *Physics Reference Manual Release 10.6* p 401

[59] Koning A J and Rochman D 2012 Modern nuclear data evaluation with the TALYS code system *Nucl. Data Sheets* **113** 2841–934